Analysis of Dynamic Charging Performances of Optimized Inductive Power Transfer Couplers

Shi, Wenli; Grazian, Francesca; Bandyopadhyay, Soumya; Dong, Jianning; Soeiro, Thiago B.; Bauer, Pavol

DOI
10.1109/PEMC48073.2021.9432541

Publication date
2021

Document Version
Final published version

Published in
2021 IEEE 19th International Power Electronics and Motion Control Conference (PEMC)

Analysis of Dynamic Charging Performances of Optimized Inductive Power Transfer Couplers

Wenli Shi, Francesca Grazian, Soumya Bandyopadhyay, Jianning Dong, Thiago B. Soeiro, Pavol Bauer
Dept. Electrical Sustainable Energy, DCE&S group
TU Delft, Mekelweg 04, 2628 CD, Delft, the Netherlands

E-mail: (W.Shi-3, F.Grazian, S.Bandyopadhyay-1, J.Dong-4, T.BatistaSoeiro, P.Bauer)@tudelft.nl

2021 IEEE 19th International Power Electronics and Motion Control Conference (PEMC) | 978-1-7281-5660-6/20/$31.00 ©2021 IEEE | DOI: 10.1109/PEMC48073.2021.9432541

***Abstract*—This paper aims to investigate the dynamic charging performance of an 11 kW dynamic inductive power transfer (DIPT) system. First, a multi-objective optimization (MOO) method is proposed to find the Pareto front of the DD charging pad. Then, the optimal design with a 96.82% efficiency is selected as the target design for the DIPT system. Based on the coupler mutual inductance at different misalignment, the orientation of the transmitter (Tx) and receiver (Rx) pads and the distance between Tx pads are studied and optimized. To obtain the dynamic characteristics of the DIPT system, the impact of mutual inductance variation is investigated, and a dynamic model using Laplace phasor transformation is built to solve the waveform amplitude of electrical variables. Finally, a time-variant circuit model is built. Based on the simulations, the dynamic model is proved to be accurate, and the proposed DIPT system displays a good dynamic charging performance.**

Keywords—dynamic inductive power transfer, multi-objective optimization, dynamic modelling method, dynamic characteristics

I. Introduction

In inductive power transfer (IPT) systems, the energy transferred from the transmitter (Tx) to the receiver (Rx) pads relies on the magnetic coupling. A high coupling is favourable for the efficiency of high power applications since less Tx side winding current is required [1]. As a price of high coupling, the size of charging pads may be designed larger and, consequently, becomes more costly. The misalignment tolerance can also be improved by enlarging the size of the charging pad. Considering the fact that the allowed construction volume is limited on the EV side, a trade-off emerges among the power transfer efficiency, power density as well as misalignment tolerance. Therefore, a multi-objective optimization (MOO) design is recommended for an IPT system.

A comprehensive comparison is reported between the double-D (DD) and rectangular charging pads in [2], where the Pareto fronts among different aspects of system performance are obtained. A broader study of different charging pad topologies is implemented in [3], where circular, rectangular, DD and DD-Quadrature (DDQ) charging pads are evaluated. The optimal efficiency is attained by adopting dual-side control [4], where two dc/dc converters are deployed on Tx and Rx sides, respectively. These two dc/dc converters are controlled to realize power regulation and impedance matching for maximum system efficiency.

Usually, the system performance at the perfectly aligned pads point plays a dominant role in the static IPT system design. In contrast, the performances of dynamic IPT (DIPT) systems are equally important at each point within the range of the misalignment in the electric vehicle (EV) travelling direction. Thus, a flat and high coupling is preferred when the EV moves along the lane in DIPT systems. However, considering the relatively large operation range of DIPT applications, the MOO loop may dramatically increase, regardless of the deployment of Tx pads, selection of movement trajectory and control of the power supply. It may be practical to implement MOO for a static scenario, taking the misalignment tolerance into account, and optimizing the Tx side configurations based on the charging pad obtained from the MOO.

In DIPT systems major technical challenges are the inevitable fluctuation of mutual coupling, power pulsation minimization [5], [6] and modelling of the dynamic characteristics [7]–[10]. To eliminate the zero-coupling point, DD couplers are overlapped [5], [6], while the material cost is high. A compromise could be realized by investigating the misaligned coupling and optimizing the distance between one Tx pad to another. Depends on the compensation topology, the order of the ac link ranges from four [7]–[9] to eight [10]. However, the modelling is mostly for time-constant systems where the mutual inductance is fixed. As the DIPT system is a time-variant system, the feasibility of the existing dynamic modelling method should be studied, which makes it essential to investigate the system dynamic characteristics and time charging rate of the mutual coupling.

This paper first implements the MOO of an 11 kW IPT coupler for static applications, and objectives include the gravimetric power density, system efficiency and misalignment tolerance. Then, the optimized coupler is analysed in terms of its mutual inductance and winding current at different misalignment conditions. Then, the optimized coupler is used to investigate the deployment configuration of the DIPT system. To analyse the transient characteristics of the DIPT system, the impact of mutual inductance variation is investigated, and a dynamic model is built. Finally, simulation is conducted to verify the accuracy of the dynamic model and validate the performances of the proposed DIPT system.

II. MOO Design

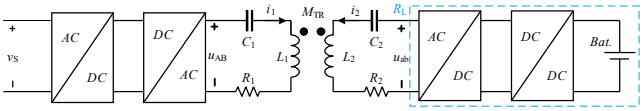

Fig. 1. Schematic of the studied IPT system

A. Power Losses Modeling

To obtain the dc input-to-dc output efficiency, power losses of the IPT system components are modelled, including power converters (inverter and rectifier), capacitors, and charging pads consisting of litz wires, ferrite cores, and aluminium shielding.

978-1-7281-5660-6/21/$31.00 ©2021 IEEE

The Litz wire loss P_{cu} is composed of the dc ohmic loss P_{dc} and the ac losses led by skin effect P_{skin} and proximity effect $P_{prox,tot}$ (internal $P_{prox,int}$ and external $P_{prox,ext}$).

$$\begin{cases} P_{dc}+P_{skin}=n_{str}r_{dc}F_R(f_o)(\dfrac{\hat{I}}{n_{str}})^2 L_{coil} \\ P_{prox,\text{int}}=n_{str}r_{dc}G_R(f_o)\dfrac{\hat{I}^2}{2\pi^2 d_a^{\,2}}L_{coil} \\ P_{prox,\text{ext}}=\sum_{i=1}^{N} n_{str}r_{dc}G_R(f_o)\int_{l_i}\hat{H}_{ext}(l)^2\,dl \end{cases} \quad (1)$$

where n_{str} is the number of strands in the litz wire, r_{dc} is the dc resistance per unit length of a unit strand of the litz wire, d_a is the diameter of the litz wire, H_{ext} is the external magnetic field penetrating the individual coil turns, f_o is the operating frequency set to be 85 kHz, $F_R(f_o)$ and $G_R(f_o)$ are frequency-dependent factors.

The ferrite core loss P_{fe} is calculated by using Steinmetz equation and integrating it over the core volume

$$P_{fe}=\iiint_V k f_0^{\,\alpha}\hat{B}^{\beta}\,dV \quad (2)$$

where Steinmetz parameters k, α and β depend on the core material.

The aluminium shielding loss due to the eddy current is calculated using the surface current density J_S equation

$$P_{al}=\iint_A \frac{1}{2}(J_S\cdot E^*)dA \quad (3)$$

As the optimal load $R_{L,opt}$ is related to the equivalent ac resistance R_{ac} of the charging pads, and R_{ac} is calculated

$$R_{ac}=\frac{P_{cu}+P_{fe}+P_{al}}{I_{rms}^{\,2}} \quad (4)$$

Then, $R_{L,opt}$ can be obtained using (5) when the series-series (SS) compensation is applied [11]. The ac link efficiency changes at different load resistance and peaks when $R_{L,opt}$ is attained as shown in Fig. 2.

$$R_{L,opt}=\omega M\sqrt{\frac{R_{ac2}}{R_{ac1}}} \quad (5)$$

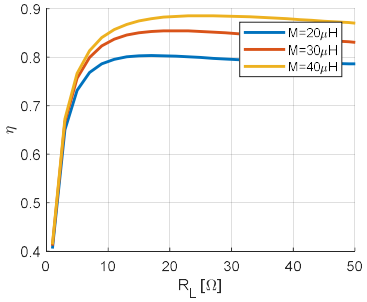

Fig. 2. The ac link efficiency under constant output power of a SS compensated IPT system

The full-bridge inverter consists of four SiC power MOSFETs (Cree C2M0040120D). The rectifier is comprised of four SiC freewheeling diodes (Cree C4D40120D). The conduction and switching losses of the MOSFETs and diodes are calculated according to [12] and the manufacturer's datasheet.

Based on the modeling method, the MOO aided by particle swarms optimization (PSO) is validated. The PSO is realized in Matlab, and the finite element (FE) models are built in COMSOL.

B. *Validation of FE Model Accuracy*

To verify the accuracy of the model approach, the magnetic parameters of the FE model built in COMSOL are benchmarked with a DD coupler, as shown in Fig. 3. The specifications of the DD coupler are listed in Table I. The magnetic parameters are measured by an impedance analyser (Agilent 4294A, 40 Hz to 110 MHz). It can be observed from Fig. 4 that both self-inductance and mutual inductance are calculated accurately by the FEM model. The error of self-inductance estimation is around 1%, and that of the mutual inductance is below 3%, which means COMSOL could accurately compute the magnetic parameters of charging pads.

TABLE I. SPECIFICATIONS OF THE DD COUPLER

Part	Property
Magnetic Core	Material: Ferrite N87 Number of bars: 3
Litz wire	Type: AWG 41 Number of strands: 525
Coil	Number of turns: 30

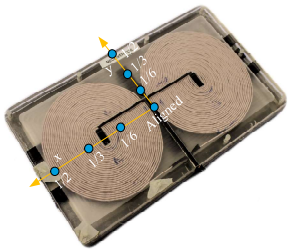

Fig. 3. 2.5 kW DD coupler

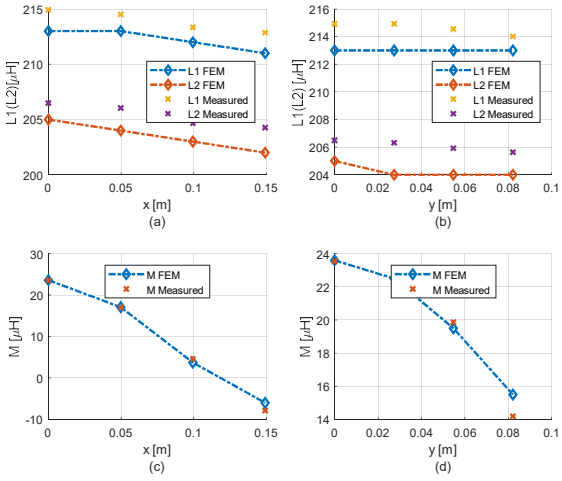

Fig. 4. Calculated and measured magnetic parameters of the coupler under misalignment, (a) and (b) self-inductance, (c) and (d) mutual inductance

C. Results

The MOO applies COMSOL to compute the magnetic field and analytically calculates the power losses of the IPT system according to the introduced power losses modelling method. The optimized target is an 11 kW DD coupler applying SS compensation. The objectives include aligned efficiency, misaligned efficiency and area/gravimetric power density. The MOO design search space and constrains are listed in Table II and III, respectively.

The MOO gives 321 sets of designs delivering an aligned efficiency higher than 93% and the highest is found to be 96.82%. Pareto fronts among design objectives are illustrated in Fig. 5. It can be seen that the aligned/misaligned efficiency present trade-offs with the gravimetric/area power density. The price of higher efficiency is a larger size of the coil and more cost of the material. By enlarging the pad size, higher coupling coefficient can be obtained. With the output power constant, the high coupling leads to decrement of winding current, thus lower power losses in the IPT system. When the power density is fixed, designs of high mutual inductance tend to be more efficient, as presented by the colour of points in Fig. 5. Besides, enlarging the pad size also boosts the misalignment tolerance of the IPT system. With the pad size increased, the variation of the mutual inductance is less sensitive to the misalignment.

Improving the power transfer efficiency is still prioritized in the design considerations. In terms of the system efficiency, two designs are highlighted as AD and BD in Fig. 5. It can be seen that they are on all these four Pareto fronts, both of which deliver good performance in aligned and misaligned points. BD is slightly inferior to AD in aligned efficiency while keeping a higher power density and misaligned efficiency. In a DIPT system, the charging performances at aligned and misaligned are equally important. Therefore, BD is selected as the optimal solution of the 11 kW DD pad design.

TABLE II. MOO SEARCH SPACE

Variable	Unit	Range	Optimal Solution
Number of turns	-	15-60	31/31
Diameters of litz wire	mm	2.4-4.8	4.8
Inner length	mm	10-35	31.9/28
Inner width	mm	10-35	25/13.3
Ferrite thickness	mm	5-35	34
Ferrite width	mm	15-45	15.8
Gap between ferrites	%	20-100	20/43.7
Length of ferrite	%	50-120	112.1/112.3
Number of ferrites	-	1-7	5/3

TABLE III. MOO CONSTRAINTS

Variable	Unit	Value
Maximum flux density	mT	300
Core loss density	kW/m^3	800
Aligned winding current density	A/mm^2	4.5
Misaligned winding current density	A/mm^2	6

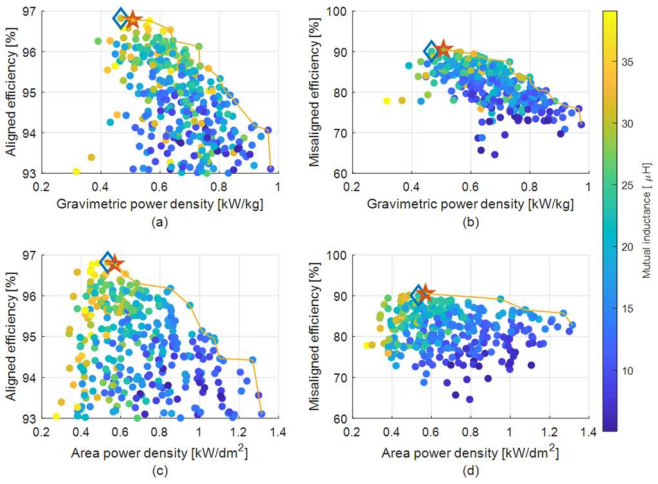

Fig. 5. Pareto fronts among objectives, (a) aligned and (b) misaligned efficiency vs. gravimetric power density, and (c) aligned and (d) misaligned efficiency vs. area power density. The design highlighted with diamond, referring as AD, has the highest aligned efficiency. The design highlighted with star, referring as BD, has the highest misaligned efficiency.

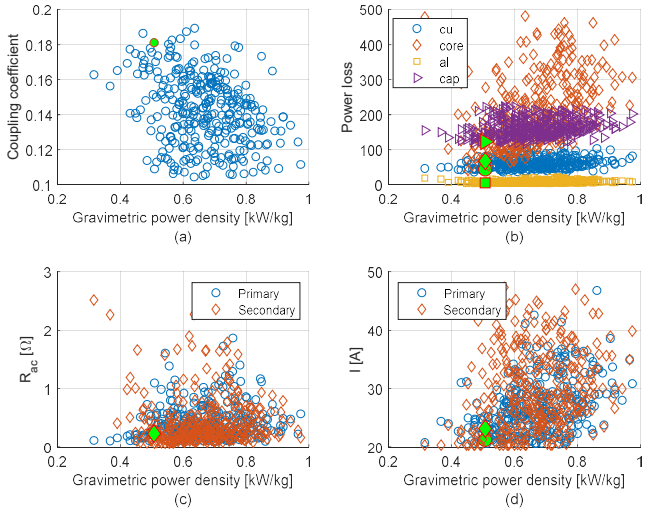

Fig. 6. System parameters (a) coupling coefficient, (b) power loss, (c) R_{ac} and (d) winding current. The selected design is highlighted using filled points.

Fig. 6 shows the system parameters of different designs, and the selected design is highlighted as filled points. The selected design has a coupling close to the highest point in Fig. 6(a). It should be noted that too high coupling coefficient may cause the load matching failure, due to the voltage limits of the dc/dc converter on both sides.

In Fig. 6(b), the aluminium shielding constitutes the lowest part of the power losses and keeps flat over the range of the power density. Usually, the thickness is selected to satisfy the skin depth, which is more sensitive on switching frequency. The copper loss takes the second-lowest place and ranges from 5% to 20%. The core loss spreads almost the whole space, and more than half of its results are above others. Compared with the core loss, capacitors have a more concentrated distribution of losses ranging from 20% to 50%. It can be concluded that capacitor and core losses have the largest power loss contribution.

R_{ac} of the primary and secondary charging pad is presented in Fig. 6(c). Most points of the primary and secondary ac resistance are overlapped and range from minimal to 2.5 Ω.

As shown in the highlighted optimal points, the optimal R_{ac} of the primary and secondary are almost the same and found around 0.2 Ω. Correspondingly, the optimal winding currents shown in Fig. 6(d) are the same with a relatively low amplitude of about 23 A in the primary and secondary sides. Therefore, keeping a balanced design might contribute to higher efficiency.

III. Tx Pads Deployment Configuration

To analyse the dynamic performances of the selected design in Section II, the coupling of the system at different relative positions are investigated. When the misalignment is relatively small, the Rx pad is only coupled with the nearest Tx pad, named ROT coupling which is used to determine the Tx pads orientation. As the Rx transits from one Tx to another, the Rx pad may have considerable coupling with two Tx pads, named RTT coupling which is used to determine the Tx pads distance.

A. Tx Pads Orientation

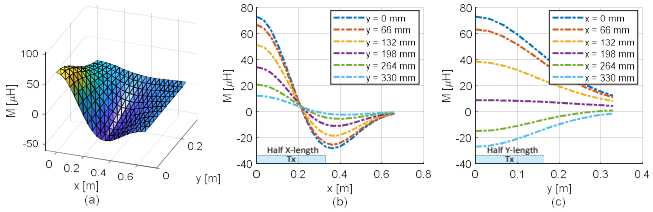

Fig. 7. ROT coupling at different positions, (a) overview, (b) x-axis misalignment and (c) y-axis misalignment. The direction of the axis is illustrated in Fig. 3.

Fig. 7 shows the mutual inductance variation at different misalignment condition. In a comparison of Fig. 7(b) and 7(c), the discussed DD coupler presents a lower sensitivity to *y*-axis misalignment, while a considerable mutual inductance can be maintained at a larger region of *x*-axis misalignment. Due to the property of DD pads, the mutual inductance has a zero-crossing point along x misalignment. The zero-crossing point is close to where one Tx D coil is aligned with one Rx D coil at a certain x-axis misalignment. When the coupling is low, the system may be shut down because of low efficiency and high component stress.

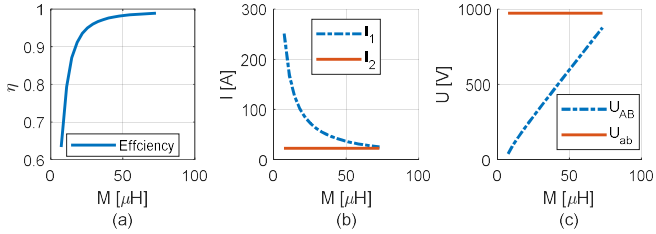

Fig. 8. DIPT system performances under different mutual inductance, (a) efficiency, (b) winding currents, and (d) input and output voltage.

When the SS compensation is applied, the system operation heavily depends on the mutual inductance. To study how to place the charging pads, the system operation should be elaborated. Assuming that the load resistance is constant and primary power regulation is applied. The output power can be regulated at 11 kW by adjusting the input voltage as

$$P_{out} = \frac{1}{2}\frac{|U_{AB}|^2}{\omega^2 M^2} R_L \tag{6}$$

where U_{AB} is the amplitude of the primary resonant circuit input voltage, R_L is the equivalent load resistance derived by the ratio between the output voltage and load current. The system performances under different mutual inductance are shown in Fig. 8. As the EV leaves the aligned point, the system efficiency decreases, and the component stresses increase. Therefore, the primary power supply should stop when the mutual inductance becomes too low. According to the SAE J2958 standard, IPT systems are required to operate with an efficiency above 80%. As a recommendation, the Tx pad power supply should stop when M_{TR} is lower than 20 μH (M_{TR_off}). Comparing the curves in Fig. 8(b) and 8(c), the *y*-misalignment provides a larger effective operation range where $M_{TR}>M_{TR\_off}$ is satisfied, even though the mutual inductance distributes in a larger range of *x*-misalignment. Therefore, the travelling direction of EVs is set to be the *y*-axis of the DD coupler.

B. Tx Pads Distance

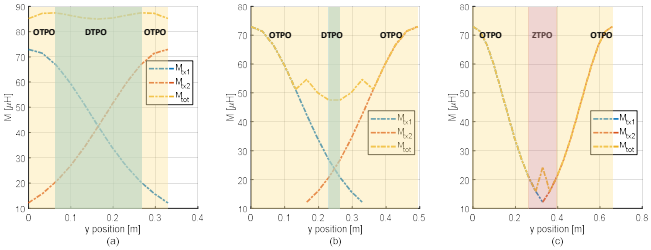

Fig. 9. RTT coupling at different postions when Tx pad distance satisfy (a) d=0, (b) d=0.5 and (c) d=1.

The pattern of the mutual inductance variation is largely affected by the distance between two adjacent Tx pads d which is defined as the ratio of the Tx pads gap and the width of the Tx pad. Fig. 7 presents the coupling when the Rx pad moves from one aligned point to another adjacent one, and also the power supply operation modes which include one Tx pad operation (OTPO), double Tx pad operation (DTPO) and zero Tx pad operation (ZTPO). DTPO presents when d ranges from 0 to 0.5, and DTPO mostly works under low mutual coupling. As shown in Fig. 8(a), the efficiency drops dramatically at low mutual inductance region. Thus, both Tx pads have relatively low efficiency in DTPO mode, which suggests that DTPO mode is not favourable in the DIPT system. Meanwhile, ZTPO should be eliminated to reduce power pulsation. Therefore, d is selected around 0.5, where both DTPO and ZTPO are avoided.

IV. Dynamic Characteristics

A. Impact of Mutual Inductance Variation

When the trajectory and speed of the EV are known, the mutual inductance can be defined as a function of time $M_{TR}(t)$ as shown in Fig 10(a). The Rx pad induced voltage V_2 can be calculated

$$V_2(t) = \omega |I_1| M_{TR}(t) \cos \omega t + M_{TR}(t)' |I_1| \sin \omega t \tag{7}$$

The second term of (7) represents induced voltage contributed by the relative motion. The ratio A_{dy} between the amplitude of the first and second terms in (7) can be expressed as

$$A_{dy} = \frac{\omega M_{TR}(t)}{M_{TR}(t)'} \tag{8}$$

When the condition $A_{dy}>>1$ is satisfied, the induced voltage resulted from the motion can be neglected. As shown in Fig. 10(b), A_{dy} is larger than 2950 at the investigated range.

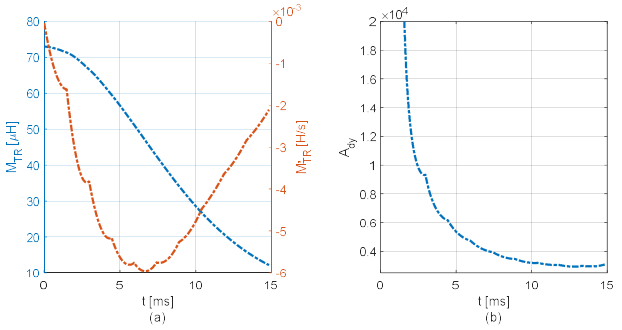

Fig. 10. Time changing rate of the mutual inductance at a speed of 80 km/h. The time for the EV to move 0.33 m (the Y length of Tx pad) is around 15 ms.

B. Dynamic Model

The conventional state-space model takes both amplitude and phase of the winding current and capacitor voltage, while the amplitude is more important for the evaluation of system efficiency, power transferred and component stresses. In [13], Laplace phasor transformation is proposed to derive the amplitude and phase of a sinusoidal electrical variable. In the Laplace phasor transformation model, the circuit is modelled in phasor domain, and the instantaneous variable x and its phasor X satisfy equation (9). The SS compensated IPT system can be modelled as (10), and the Laplace phasor transformed equivalent circuit is presented in Fig. 11. In (10), U_{C1}, I_1, U_{C2} and I_2 are the phasor transformation of instantaneous u_{C1}, i_1, u_{C2} and i_2, U_{AB} is the fundamental component of instantaneous u_{AB}.

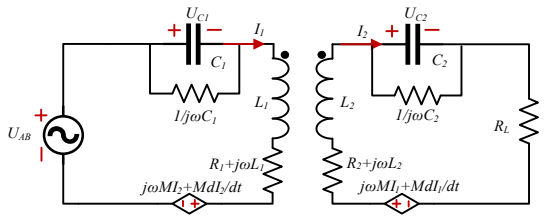

Fig. 11. Laplace phasor transformed equivalent circuit model.

$$x = \mathrm{Re}[Xe^{j\omega t}] \tag{9}$$

$$\begin{cases} U_{AB} = L_1\dfrac{dI_1}{dt} + (R_1 + j\omega L_1)I_1 + M\dfrac{dI_2}{dt} + j\omega MI_2 + U_{C1} \\ I_1 = \dfrac{U_{C1}}{j\omega C_1} + C_1\dfrac{dU_{C1}}{dt} \\ M\dfrac{dI_2}{dt} + j\omega MI_2 = L_2\dfrac{dI_2}{dt} + (j\omega L_2 + R_2 + R_L)I_2 + U_{C2} \\ I_2 = \dfrac{U_{C2}}{j\omega C_2} + C_2\dfrac{dU_{C2}}{dt} \end{cases} \tag{10}$$

To simplify (10), it is assumed that the phase angle between U_{C1} (U_{C2}) and I_1 (I_2) is 90 degree, and U_{AB} and I_1 are in phase. Thus, the open-loop transfer function between $|I_1|(s)$ and $|U_{AB}|(s)$ can be solved as

$$\frac{|I_1|(s)}{|U_{AB}|(s)} = \frac{2L_2 s + R_2 + R_L}{4L_1L_2 s^2 + 2((R_2+R_L)L_1 + L_2R_1)s + (R_2+R_L)R_1 + \omega^2 M_{TR}^2} \tag{11}$$

The decaying rate τ_d can be solved as

$$\tau_d = \frac{R_1L_2 + (R_2+R_L)L_1}{4L_1L_2} \tag{12}$$

Assuming the transient component decays to 5%, the transient time t_d can be solved

$$t_d = \frac{4\pi L_1L_2}{R_1L_2 + (R_2+R_L)L_1} \tag{13}$$

The mutual inductances are not involved in (13), which means the t_d is constant as the EV passes the Tx pad. The step response of the discussed system has a t_d of 0.12 ms. According to Fig. 10(a), the variation of M_{TR} during the transient time t_d is less than 1.2 μH, which is negligible to the DIPT system. Thus, a feed-forward control is capable of reaching a relatively stable output power.

V. Simulation Results

A. Dynamic Response under Constant M_{TR}

To verify the accuracy of the proposed dynamic model, the circuit model is built in Simulink. The model details are listed in Table III. The pad details are derived from MOO results. The optimal load resistance is applied, which is calculated to be around 43 Ω, according to (5). The waveform of the primary winding current under 400 V input voltage step is illustrated in Fig. 12. The analytical prediction is based on (11). The analytical curve fits the simulated waveform perfected and the transient time is around 0.12 ms, which proves the accuracy of the proposed dynamic model in (10) and the simplified analytical solution in (11).

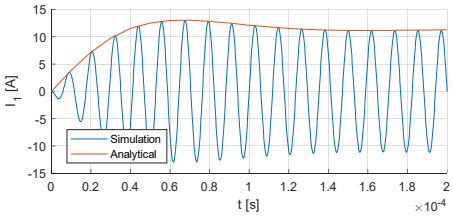

Fig. 12. Comparison of simulated and analytical results under 400V step U_{AB} and M_{TR} constant.

TABLE IV. Simulation Model Details

Variable	Unit	Value
L_1	μH	504.7
L_2	μH	425.6
M_{TR}	μH	72.9
C_1	nF	6.95
C_2	nF	8.24
R_1	Ω	0.2
R_2	Ω	0.25

B. Dynamic Response under Varying M_{TR}

According to Section III, the distance between adjacent Tx pads is around half of the Tx pad Y-length. In that case, the effective charging zone can be continued, and the overall power efficiency can be guaranteed above 80%. When the lateral misalignment is zero, the coupling between the Rx pad and Tx$_k$ pad is illustrated in Fig. 13. Under the condition that the EV trajectory and speed are fixed, the M_{TR} can be

predicted. According to Section IV, the variation of M_{TR} during transient time is negligible. Therefore, the primary side power regulation can be achieved using feed-forward control strategy. Taking the constant output power as the target, the primary input voltage can be controlled as

$$\left|U_{AB}\right| = \omega M_{TR}\sqrt{2P_{out,r} / R_L} \tag{14}$$

where $P_{out,r}$ is the rated output power 11 kW.

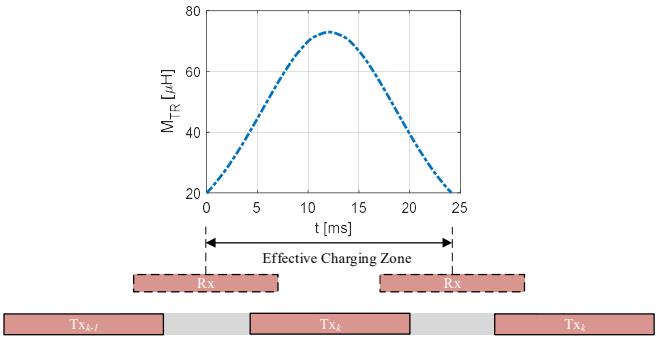

Fig. 13. M_{TR} between Rx pad and Tx_k pad as the EV enters and leaves the effective charging zone at the speed of 80 kM/h. The lateral misalignment is assumed to be zero. At both ends of the effective charging zone, M_{TR} is 20 μH.

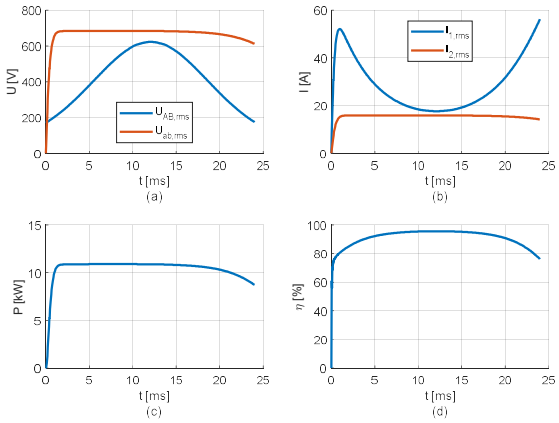

Fig. 14. Dynamic performance under the primary power regulation using feed-forward control strategy. (a) RMS value of input and output voltage, (b) rms value of primary and secondary winding current, (c) output power, (d) AC link power efficiency.

To simulate the performances of DIPT system over the effective charging zone, a time-variant circuit model is built. The mutual inductance charges as Fig. 13. The dynamic performances of the DIPT system over the effective charging zone are presented in Fig. 14. As per Fig. 14(b), the start-up transient of I_2 lasts around 1 ms, resulting from the transient characteristics of the resonant circuit and the variation of M_{TR}. After the start-up transient, the I_2 becomes stable, and the variation of M_{TR} is compensated by adjusting U_{AB} through the feed-forward control strategy as (14). As per Fig. 14(d), the system efficiency is lower than 80% when the EV is at the ends of the effective charging zone. This is because the load resistance is fixed to be the optimal load when the EV is aligned with the Tx pad.

VI. Conclusions

This paper implements a MOO design of an 11 kW IPT DD coupler. The MOO applies FEM tool to compute the magnetic field and analytically calculates the power losses of the IPT system. Based on the Pareto front obtained, an optimal solution is selected to design a DIPT system. By investigating the mutual coupling at different misalignment, the deployment of the Tx pads is investigated. It has been found that the mutual coupling is less sensitive when the *y*-axis of the coupler is set to be the travelling direction of the EV. To avoid null power and low-efficiency operation region, the suitable distance between two adjacent Tx pads is found to be roughly half the Y-length of the Tx pad. Based on the configuration of the DIPT system, the impact of mutual inductance variation is studied, and a dynamic model using Laplace phasor transformation is built. Based on the dynamic model, the open-loop transfer function is derived, and the time-domain solution is solved. Finally, a time-variant circuit model is built. The simulation results validate the accuracy of the dynamic model and performances of the DIPT system using the proposed pad design and deployment configuration.

References

[1] R. Bosshard and J. W. Kolar, "Multi-Objective Optimization of 50 kW/85 kHz IPT System for Public Transport," *IEEE Journal of Emerging and Selected Topics in Power Electronics*, vol. 4, no. 4, pp. 1370–1382, Dec. 2016, doi: 10.1109/JESTPE.2016.2598755.

[2] R. Bosshard, U. Iruretagoyena, and J. W. Kolar, "Comprehensive Evaluation of Rectangular and Double-D Coil Geometry for 50 kW/85 kHz IPT System," *IEEE Journal of Emerging and Selected Topics in Power Electronics*, vol. 4, no. 4, pp. 1406–1415, Dec. 2016, doi: 10.1109/JESTPE.2016.2600162.

[3] S. Bandyopadhyay, P. Venugopal, J. Dong, and P. Bauer, "Comparison of Magnetic Couplers for IPT-Based EV Charging Using Multi-Objective Optimization," *IEEE Transactions on Vehicular Technology*, vol. 68, no. 6, pp. 5416–5429, Jun. 2019, doi: 10.1109/TVT.2019.2909566.

[4] T. Diekhans and R. W. D. Doncker, "A Dual-Side Controlled Inductive Power Transfer System Optimized for Large Coupling Factor Variations and Partial Load," *IEEE Transactions on Power Electronics*, vol. 30, no. 11, pp. 6320–6328, Nov. 2015, doi: 10.1109/TPEL.2015.2393912.

[5] S. Cui, Z. Wang, S. Han, C. Zhu, and C. C. Chan, "Analysis and Design of Multiphase Receiver with Reduction of Output Fluctuation for EV Dynamic Wireless Charging System," *IEEE Transactions on Power Electronics*, pp. 1–1, 2018, doi: 10.1109/TPEL.2018.2859368.

[6] Y. Liu, R. Mai, D. Liu, Y. Li, and Z. He, "Efficiency Optimization for Wireless Dynamic Charging System With Overlapped DD Coil Arrays," *IEEE Transactions on Power Electronics*, vol. 33, no. 4, pp. 2832–2846, Apr. 2018, doi: 10.1109/TPEL.2017.2751593.

[7] H. Li, K. Wang, L. Huang, W. Chen, and X. Yang, "Dynamic Modeling Based on Coupled Modes for Wireless Power Transfer Systems," *IEEE Transactions on Power Electronics*, vol. 30, no. 11, pp. 6245–6253, Nov. 2015, doi: 10.1109/TPEL.2014.2376474.

[8] H. Li, J. Fang, and Y. Tang, "Dynamic Phasor-Based Reduced-Order Models of Wireless Power Transfer Systems," *IEEE Transactions on Power Electronics*, vol. 34, no. 11, pp. 11361–11370, Nov. 2019, doi: 10.1109/TPEL.2019.2897823.

[9] S. Lee, B. Choi, and C. T. Rim, "Dynamics Characterization of the Inductive Power Transfer System for Online Electric Vehicles by Laplace Phasor Transform," *IEEE Transactions on Power Electronics*, vol. 28, no. 12, pp. 5902–5909, Dec. 2013, doi: 10.1109/TPEL.2013.2254500.

[10] W. Shi, J. Deng, Z. Wang, and X. Cheng, "The Start-up Dynamic Analysis and One Cycle Control-PD Control Combined Strategy for Primary-Side Controlled Wireless Power Transfer System," *IEEE Access*, vol. 6, pp. 14439–14450, 2018, doi: 10.1109/ACCESS.2018.2811179.

[11] S. Bandyopadhyay, P. Venugopal, J. Dong, and P. Bauer, "Comparison of Magnetic Couplers for IPT-Based EV Charging Using Multi-Objective Optimization," *IEEE Transactions on Vehicular Technology*, vol. 68, no. 6, pp. 5416–5429, Jun. 2019, doi: 10.1109/TVT.2019.2909566.

[12] K. Peng and E. Santi, "Performance projection and scalable loss model of SiC MOSFETs and SiC Schottky diodes," in *2015 IEEE Electric Ship Technologies Symposium (ESTS)*, Jun. 2015, pp. 281–286, doi: 10.1109/ESTS.2015.7157905.

[13] C. T. Rim and G. H. Cho, "Phasor transformation and its application to the DC/AC analyses of frequency phase-controlled series resonant converters (SRC)," *IEEE Transactions on Power Electronics*, vol. 5, no. 2, pp. 201–211, Apr. 1990, doi: 10.1109/63.53157.